Chinese Chemical Letters 36 (2025) 110300

Contents lists available at ScienceDirect

Chinese Chemical Letters

journal homepage: www.elsevier.com/locate/cclet

Stable core-shell Janus BiAg bimetallic catalyst for CO_2 electrolysis into formate

Yaoyin Lou[a,c], Xiaoyang Jerry Huang[b,d], Kuang-Min Zhao[c], Mark J. Douthwaite[b], Tingting Fan[c], Fa Lu[c], Ouardia Akdim[b,*], Na Tian[c], Shigang Sun[c,d,*], Graham J. Hutchings[b,*]

[a] CAS Key Laboratory of Urban Pollutant Conversion, Institute of Urban Environment, Chinese Academy of Sciences, Xiamen 361021, China
[b] Max Planck-Cardiff Centre on the Fundamentals of Heterogeneous Catalysis FUNCAT, Cardiff Catalysis Institute, School of Chemistry, Cardiff University, Cardiff CF10 3AT, United Kingdom
[c] State Key Laboratory of Physical Chemistry of Solid Surfaces, Department of Chemistry, College of Chemistry and Chemical Engineering, Xiamen University, Xiamen 361005, China
[d] Center of Advanced Electrochemical Energy, Institute of Advanced Interdisciplinary Studies, Chongqing University, Chongqing 400044, China

ARTICLE INFO

Article history:
Received 28 February 2024
Revised 18 July 2024
Accepted 26 July 2024
Available online 27 July 2024

Keywords:
CO_2 reduction
Cascade catalysis
Formate
BiAg
Janus

ABSTRACT

CO_2 electrolysis into formate is a promising technology with the potential to simultaneously alleviate energy shortages and global warming. However, the limited stability of the catalysts during long-term electrolysis hinders their widespread implementation. Herein, we show that a core-shell bimetallic BiAg catalyst with a multifaceted Janus structure at its core can achieve a stability of up to 300 h with a formate faradaic efficiency ($FE_{formate}$) over 90% at −0.75 V *vs.* RHE (reversible hydrogen electrode) in an H-type cell. Our investigations reveal the important role of the Janus structure on the transfer of electrons, favoring their delocalization across the catalyst and enhancing their mobility. We propose that the compressive strain inclined to grain boundaries within this structure would lower the energy barrier for electrons transfer and promotes the cooperation between Ag and Bi. Indeed, Ag initiates the activation of CO_2 through a series of cascade reactions and is subsequently hydrogenated on Bi. Additionally, our study suggests that Ag plays a crucial role in stabilizing the catalyst structure after long-term electrolysis. This work highlights a new strategy for tandem CO_2 electrolysis, providing novel insights for the design of formate formation catalysts.

© 2025 Published by Elsevier B.V. on behalf of Chinese Chemical Society and Institute of Materia Medica, Chinese Academy of Medical Sciences.

The excessive consumption of fossil fuels results in significant anthropogenic CO_2 emissions, contributing to the greenhouse effect and subsequent global warming. Recognizing this pressing challenge, governments worldwide have made commitments to achieve net zero carbon emissions by 2050 [1]. To address this target, one effective route focuses on carbon recycling which involves transforming CO_2 into value-added chemicals or low carbon fuels [2–5]. CO_2 electroreduction reaction (eCO_2RR), powered by renewable electricity sources, holds great potential to achieving a CO_2-neutral energy cycle. Recent techno-economic analyses have underscored formate (or formic acid) as the most valuable product of eCO_2RR per mole of electrons (16.1×10^{-3} $/electron) [6]. Indeed, formate finds widespread application in various industries, including pharmaceuticals, textiles, and as hydrogen carrier fuel [7,8].

The efficiency of eCO_2RR is often limited by the use of aqueous electrolyte solutions, due to the competitive hydrogen evolution reaction (HER) which tends to consume a significant portion of the input charge. Therefore, achieving high selectivity for the desired product is crucial to avoid wasting electricity on undesired byproducts. With its low HER activity and high free energy for hydrogen adsorption, bismuth (Bi) emerges as a promising and cost-effective electrocatalyst for high $FE_{formate}$. Extensive efforts were devoted to fine-tuning the composition, size, and morphology of Bi catalysts in order to achieve high activity [9,10]. More recently, Bi-based bimetallic catalysts were developed to enhance the eCO_2RR activity, leveraging the synergistic geometric and electronic effects between heterometallic components [11–13]. Although some of these catalysts have achieved a $FE_{formate}$ over 95%, they are associated with a poor stability and a narrow potential window wherein 90% $FE_{formate}$ is maintained. Furthermore, a high stability during the electrolysis is also a major parameter to consider for the viability of the process. Hence, it is imperative to explore and identify more

* Corresponding authors.
E-mail addresses: akdimo@cardiff.ac.uk (O. Akdim), sgsun@xmu.edu.cn (S. Sun), hutch@cardiff.ac.uk (G.J. Hutchings).

https://doi.org/10.1016/j.cclet.2024.110300
1001-8417/© 2025 Published by Elsevier B.V. on behalf of Chinese Chemical Society and Institute of Materia Medica, Chinese Academy of Medical Sciences.

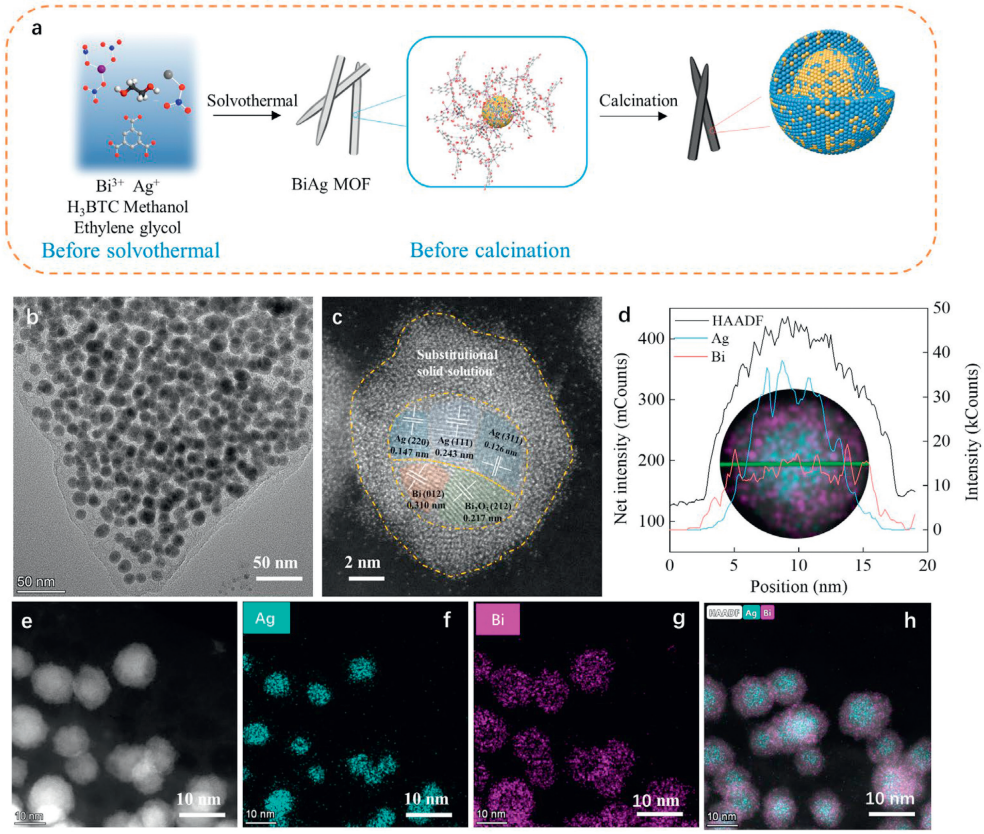

Fig. 1. (a) Synthesis route for BiAg-600. (b) HRTEM image of BiAg-600. (c) AC-STEM of an individual nanoparticle of BiAg-600. (d) Compositional line profiles of Bi (red) and Ag (blue) recorded along the arrow shown in the HAADF-STEM image. (e-h) Energy dispersive X-ray spectroscopy elemental mappings of BiAg-600.

promising electrocatalysts to effectively address these challenges in the context of large-scale implementation.

Positively, our catalyst maintains a $FE_{formate}$ of over 90% across an 860 mV potential window, while remaining stable during 300 h at −0.75 V *vs.* RHE. To unveil the fundamental factors responsible for the remarkable stability of our catalyst, we have conducted physicochemical characterization revealing the pivotal role of the multifaceted Janus bimetallic core structure. Furthermore, the utilization of electrochemical isotopic tracing technique, electrochemical *in situ* attenuated total reflectance Fourier transformed infrared spectroscopy (ATR-FTIR) and *in situ* shell-isolated nanoparticle enhanced Raman spectroscopy (SHINERS) permitted to disclose a CO_2RR cascade mode on BiAg, where Ag sites adsorb HCO_3^- increasing the CO_2 concentration and the local pH nearby Bi sites, where the formation of $^*OCHO^-$ (with * the active site) species is promoted whilst the HER is hindered.

Building upon the distinctive characteristics of metal-organic frameworks (MOFs) [14,15], we synthesize monometallic Bi, Ag and bimetallic BiAg catalysts (Fig. 1a). The as-prepared catalysts were designated as Bi-600, Ag-600 and BiAg-600 (Note S1, Figs. S1 and S2 in Supporting information).

Scanning electronic microscopy (SEM) displayed for both Bi-based catalysts a micron-pyramidal hexagonal prism shape (Figs. S3a and b in Supporting information). High resolution transmission electron microscopy (HR-TEM) revealed that BiAg-600 nanoparticles exhibited an average particle size of 10.8 nm, encompassed by a graphitic layer measuring *ca.* 6–8 nm in thickness (Fig. S4 in Supporting information and Fig. 1b). In contrast, the Bi nanoparticles were comparatively larger, with an average size of *ca.* 50 nm, and similarly enclosed by a graphitic layer measuring 1.5 nm in thickness (Fig. S5 in Supporting information). Aberration corrected scanning electron microscopy (AC-SEM) highlighted the specific core-shell structure of Ag and Bi inside BiAg-600 (Fig. 1c). The compositional line analysis (Fig. 1d) and energy dispersive X-ray spectroscopy elemental mapping (Figs. 1e-h) demonstrated that the BiAg bimetallic shell (*ca.* 2 nm thickness) was amorphous and enriched by Bi, with a Bi/Ag ratio of *ca.* 5.4, according to X-ray photoelectron spectroscopy (XPS) (Fig. S6 in Supporting information). The core was composed of both Bi and Ag atoms with different crystal planes and with segregated phases forming multifaceted Janus nanostructures (Fig. 1c).

Within the core region, a tensile strain effect was observed for Ag (111), Ag (220), and Ag (311), with lattice spacings of 0.243 nm, 0.147 nm, and 0.126 nm, respectively. These values exceeded the standard lattice spacings, which are respectively 0.235 nm, 0.145 nm, and 0.123 nm (PDF #04–0783). This tensile strain can be attributed to Bi being approximately 5% larger than Ag [16]. Simultaneously, the interplanar spacing of the (012) rhombohedral Bi lattice plane, measured at 0.310 nm, was smaller than the standard value of 0.328 nm, indicating a compressive strain effect. This, was further supported by the absence of strain in Bi-600, where the lattice fringe for Bi (012) measured 0.328 nm, similar to the standard value (Fig. S5). These strains are inclined to grain boundaries [17].

Bi 4f and Ag 3d core-level XPS spectra were monitored (Figs. 2a-c). For BiAg-600, at the near surface region (∼10 atomic layer) [18], Ag 3d showed a doublet with a binding energy of 368.3 eV (Ag $3d_{5/2}$) and 374.3 eV (Ag $3d_{3/2}$) assigned to Ag^0 [19], while Bi 4f depicted two peaks at 164.2 eV (Bi $4f_{5/2}$) and 159.1 eV (Bi $4f_{7/2}$) assigned to the oxidation of Bi resulting from the exposition of the catalyst to air [20]. After Ar etching, two shoulder peaks appeared at 162.5 eV and 157.2 eV and were attributed to Bi^0. According to

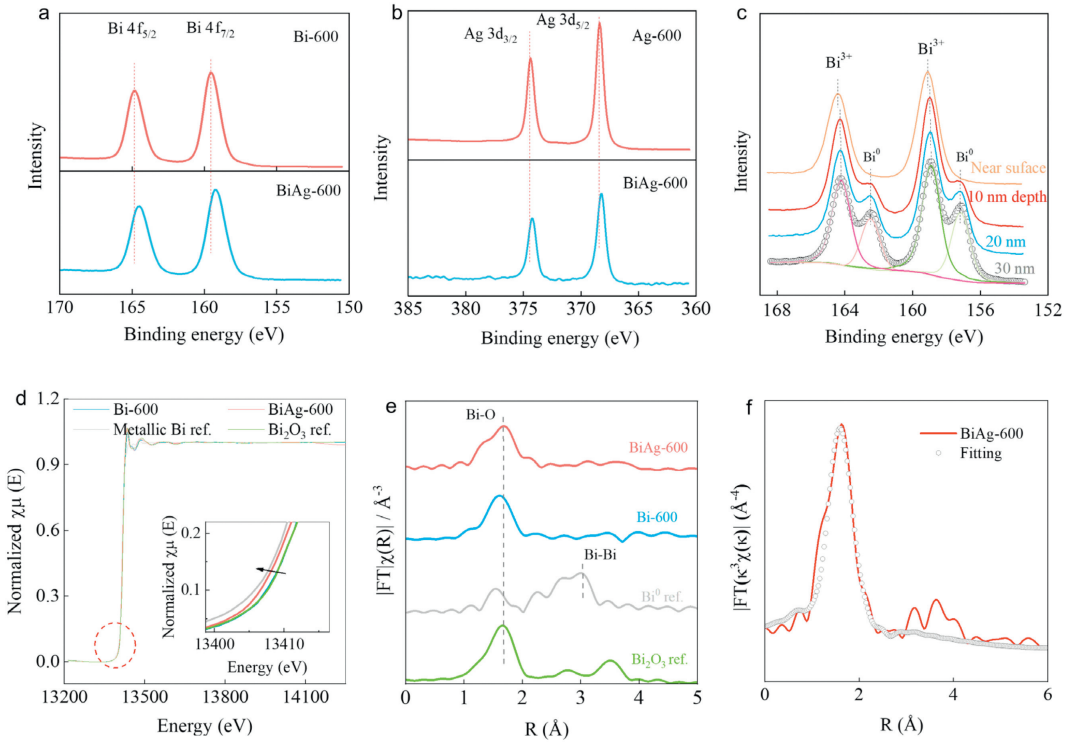

Fig. 2. Electronic properties of Bi-600 and BiAg-600. X-ray photoelectron spectroscopy spectra of BiAg-600 compared with Bi-600 (a) and Ag-600 (b). (c) XPS spectra depth profiling of BiAg-600. (d) XANES spectra of Bi L_3-edge of BiAg-600 and Bi-600, compared to the metallic Bi foil and Bi_2O_3 used as references. (e) Bi L_3-edge FT-EXAFS spectra. (f) Corresponding EXAFS fitting curves for BiAg-600 at R space.

the peak's areas, a Bi/Ag ratio of ~5.4 was obtained at the surface region, and decreased to ~1.2 at the subsurface of 30 nm (Fig. S6), confirming that BiAg-600 was enriched with Bi in the near-surface. This enrichment would be caused by the difference in surface energy between Bi and Ag, prompting the spontaneous aggregation of Bi atoms on the catalyst's surface during synthesis [21–25]. The binding energy of Bi $4f_{7/2}$ on the surface of BiAg-600 exhibited a lower value compared to Bi-600 (159.1 eV *vs.* 159.5 eV). One plausible explanation is the difference in electronegativity between Bi (2.02 eV) and Ag (1.93 eV), resulting in a higher electron density surrounding Bi atoms and consequently a lower valence state of Bi. Another contributing factor could be the compressive strain observed on Bi due to the presence of Ag, inducing a delocalization of the Bi-p orbital [26]. Moreover, the binding energy of Bi $4f_{7/2}$ within the shell exhibits a higher value compared to the core region, indicating an uneven distribution of charges among Bi atoms throughout the catalyst. This, can be attributed to a gradient concentration of Ag atoms across the BiAg-600 nanoparticles, with the core region displaying a higher enrichment of Ag (Fig. S6). As a result, the distribution of electrons across the catalyst is influenced by this varying composition within the nanoparticles. In addition, XANES spectra of Bi L3-edge (Fig. 2d) depicted a negative shift of the absorption edge position toward metallic Bi foil in the presence of Ag (black arrow in Fig. 2d), pointing to an electron transfer from Ag to Bi. Besides, the extended X-ray absorption fine structure (EXAFS) analysis (Figs. 2e and f) provided further insight by revealing that the valence state of $Bi^{\delta+}$ in BiAg-600 fell within the range of $2 < \delta < 3$ (Fig. 2e). This result was lower than that of Bi in Bi-600, which is typically +3. Furthermore, in the EXAFS spectra, the R spaces for BiAg-600 and Bi-600 presented a peak at 1.69 Å in Bi L_3-edge, corresponding to Bi-O scattering path of Bi_2O_3. The coordination numbers of Bi-O were about 2.2 and 3.2 for BiAg-600 and Bi-600 respectively, indicating that the incorporation of Ag promoted a lower coordination number (Fig. 2f and Table S1 in Supporting information).

The electrocatalytic activities of the catalysts were initially assessed in a gas-tight H-type cell, using a 0.5 mol/L $KHCO_3$ aqueous solution. A commercial Bi powder (referred to as comm. Bi) was used for comparison. From the linear sweep voltammetry (LSV), Bi-based catalysts exhibited higher current densities in the CO_2-saturated electrolyte when compared to the blank Ar-saturated solution, Fig. 3a. This, confirms a reduced activity towards HER [27]. Chronoamperometric tests were conducted at various potentials using CO_2-saturated solutions. The resulting gaseous and liquid products from 1-h electrolysis were collected and analyzed using gas chromatography (GC) and nuclear magnetic resonance (NMR) (Fig. S7 in Supporting information). Formate was found to be the primary product observed on all the Bi-based catalysts across the entire potential range, while CO and H_2 were minor products with a $FE < 5\%$. BiAg-600 demonstrated the highest efficiency with the highest $FE_{formate}$, superior current density ($j_{formate}$), and remarkable formate production rate, reaching respectively 97% at −1.3 V, 58.6 mA/cm^2 at −1.0 V, and 974 μmol cm^{-1} h^{-1} at −1.1 V (Figs. 3b and c). Bi-600 achieved a $FE_{formate}$ of 91% at −1.1 V, a $j_{formate}$ of 51.3 at −1.0 V and formate production rate of 852 μmol cm^{-1} h^{-1} at −1.0 V. The Bi comm. showed the lowest activity with a $FE_{formate}$ of 88% at −1.0 V, a $j_{formate}$ of 47.6 mA/cm^2 at −0.9 V and formate production rate of 638 μmol cm^{-1} h^{-1} at −1.0 V. Most importantly BiAg-600 was able to maintain a $FE_{formate}$ over 90% across a potential range window of 860 mV.

A smaller ECSA was observed for BiAg-600 compared to Bi-600, which can be attributed to the rougher surface exhibited by Bi-600 (Fig. 3d, Figs. S3a, b and S8 in Supporting information). The normalization of the partial current density of formate formation against ECSA ($j_{ESCA\text{-}formate}$) showed for BiAg-600 a much higher intrinsic activity with a $j_{ESCA\text{-}formate}$ of 2.3 mA/cm^2 at −1.0 V against 1.1 mA/cm^2 for Bi-600 (Fig. S9 in Supporting information).

In the same potential region, the incorporation of Ag into Bi resulted in an improved rate with a smaller Tafel slope compared to the monometallic Bi catalyst (96.9 mV/dec *vs.* 117.3 mV/dec,

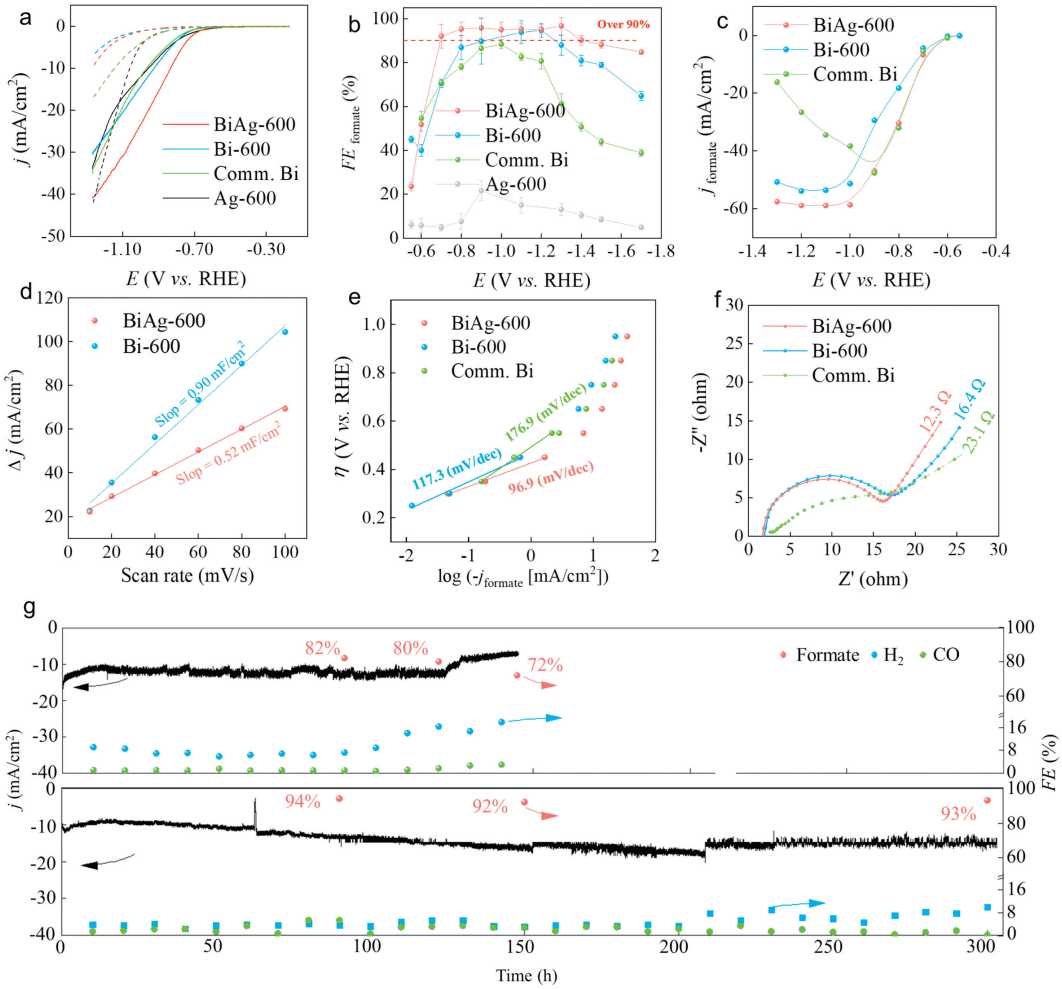

Fig. 3. CO_2 Electrolysis performances in H-type Cell of BiAg-600, Bi-600 and comm. Bi. (a) LSV curves in Ar- and CO_2-saturated 0.5 mol/L $KHCO_3$ aqueous solution. (b) Potential-dependent Faradaic efficiencies of formate in CO_2-saturated 0.5 mol/L $KHCO_3$ aqueous solution. (c) Formate partial current density generation against potential. (d) Electrochemically active surface area measurement of BiAg-600 and Bi-600; Half-charging current density differences ($\Delta j/2$) are plotted against scan rates. (e) Tafel plots obtained on BiAg-600 and Bi-600. (f) Nyquist plots obtained on BiAg-600, Bi-600 and comm. Bi. (g) Current density and $FE_{formate}$ on Bi-600 (top) and BiAg-600 (bottom) during potentiostatic tests at −0.75 V.

Fig. 3e). The data, substantiated by electrochemical impedance spectroscopy (EIS) experiments (Fig. 3f) indicated a faster electron transfer rate on BiAg-600. In addition, the Tafel slopes for both catalysts were close to the theoretical value of 120 mV/dec, suggesting that the rate-determining step (RDS) was the first electron transfer step [28]. The Bi comm. displayed a Tafel slope of 176.9 mV/dec indicative of a low activity.

BiAg-600 exhibited a remarkable level of stability, maintaining a consistently high $j_{formate}$ of 14.8 mA/cm^2 and a $FE_{formate} > 90\%$ throughout 300 h at −0.75 V (Fig. 3g). These performances, make our catalyst one of the most stable compared to state-of-the-art bismuth-based electrocatalysts in eCO_2RR for formate formation (Table S2 in Supporting information). Bi-600 displayed stability for only 122 h with negligible fluctuations in $j_{formate}$ (12.6 mA/cm^2) before experiencing a decline. Comm. Bi revealed a significantly shorter stability period of less than 20 h (Fig. S10 in Supporting information).

The performances of the BiAg-600 were further investigated in a gas diffusion electrode flow cell (Fig. S11a in Supporting information). Under these conditions, the current density recorded was greatly enhanced (Fig. S11b in Supporting information), and was ascribed to a better diffusion of CO_2. Formate started to be detected at −0.44 V, corresponding to an overpotential η of only 190 mV, and with a $FE_{formate}$ of 93.1% (Fig. S11c in Supporting information). BiAg-600 demonstrated a stable industrial relevant current density of 200 mA/cm^2 at $\eta = 300$ mV with a $FE_{formate}$ of 94.3% (Fig. S11d in Supporting information).

A linear correlation was observed between $FE_{formate}$ and the binding energies of Bi $4f_{5/2}$ for the tested catalysts (Fig. S12 in Supporting information), indicating that a more reduced oxidation state of Bi promotes the formation of formate during the reaction.

In the aim to investigate the properties responsible for the stability of BiAg-600, the structure, morphology, and electronic properties of Bi-600 and BiAg-600 were examined after reaction. SEM images showed significant damage to the structure of Bi-600 (Fig. S13a in Supporting information), while BiAg-600 structure was well preserved (Fig. S13b in Supporting information). X-ray diffraction (XRD) analysis revealed that the crystalline structures of BiAg-600 and Bi-600 remained almost unaffected after the reaction (Figs. S14a and b in Supporting information), with some changes on the crystallites sizes. While the binding energies of Ag $3d_{5/2}$ in BiAg-600 remained constant (Fig. S14c in Supporting information), the binding energies of Bi $4f_{5/2}$ and Bi $4f_{7/2}$ on the surface slightly increased by approximately 0.6 eV (Figs. S14d and e in Supporting information), but to a lesser extent compared to Bi-600, which exhibited an increase of around 2 eV (Fig. S14f in Supporting information). The morphological transformation of the catalysts can be attributed to the electromigration of Bi atoms from the bulk

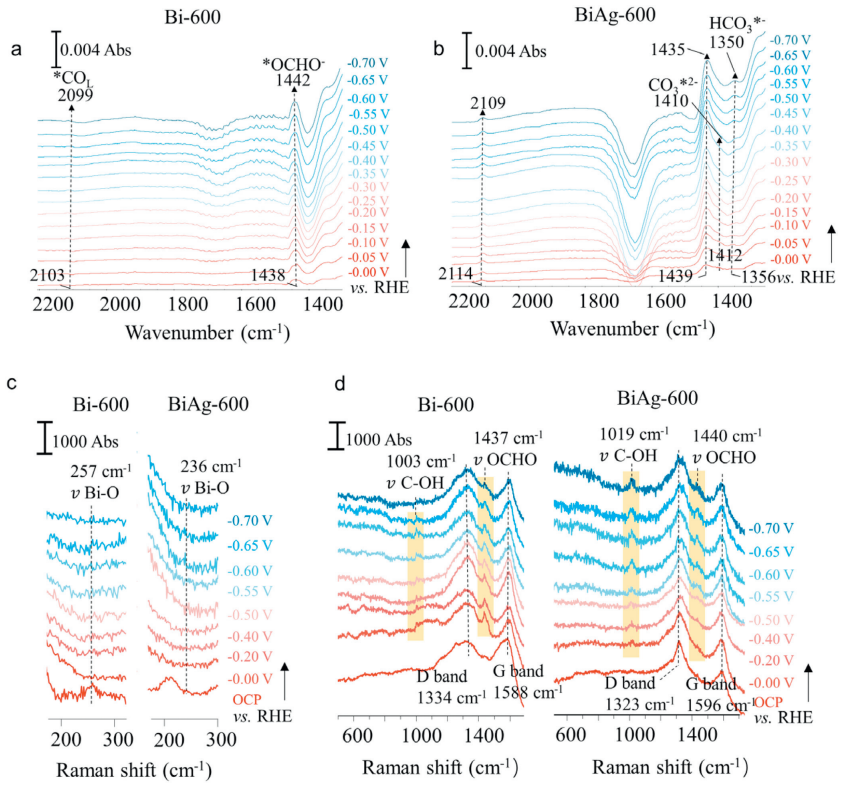

Fig. 4. Electrochemical *in situ* ATR-FTIR analysis. Bi-600 (a), BiAg-600 (b) in CO_2-saturated 0.5 mol/L $KHCO_3$ between 0.0 V and −0.7 V. *In situ* SHINERS and proposed mechanism: BiAg-600 (c) and Bi-600 (d) in CO_2-saturated 0.5 mol/L $KHCO_3$ between 0.0 V and −0.8 V.

to the surface of Bi-600 during the electrolysis process (Fig. S14f and Note S2 in Supporting information). The incorporation of Ag would stabilize Bi and contribute to the preservation of the pyramidal structure of BiAg-600. It also appears that the introduction of Ag contributed to the stabilization of the electronic properties of Bi, possibly through the presence of the compressive strain structure discussed in the characterization section.

Electrochemical *in situ* ATR-FTIR at different potential, was used on BiAg-600, Bi-600 and Ag-600 and the results were reported in Fig. 4 and Fig. S15 (Supporting information). A list of IR band assignments can be found in Table S3 (Supporting information), and detailed explanations are provided in Note S3 and Fig. S16 (Supporting information). Bridge bonded CO species ($*CO_B$) are considered as a crucial intermediate in the formation of CO during CO_2 reduction [29]. In the IR spectra, this intermediate was exclusively detected on Ag-600, explaining its high selectivity towards CO compared to Bi-based catalysts (Fig. S7d). Linear-bonded CO species ($*CO_L$) were observed on the surface of all catalysts, although the band intensity of $*CO_L$ was significantly lower for Bi-600, indicating the important role of Ag in its formation on the BiAg-600 catalyst. Notably, the IR band of $*CO_L$ on BiAg-600 exhibited a blue shift of approximately 11 cm^{-1} compared to Bi-600, which can be attributed to the presence of Ag. This shift indicates a downshift of the d-band of Bi upon the introduction of Ag [30]. Besides, the high band intensity of the *OCHO species observed on Bi-based catalysts explained their high $FE_{formate}$. Moreover, the band intensity of $*OCHO^-$ in the BiAg-600 was the highest and could be associated with the high selectivity of this catalyst toward formate formation. It is worth noting that the presence of $*OCHO^-$ and $*CO_L$ species was also observed in the spectra of BiAg-600 under Ar (Fig. S17 in Supporting information). This, suggests that HCO_3^- from the electrolyte may play a role in the formation of formate and CO during the eCO_2RR process. Furthermore, the fact that HCO_3^{*-} was only present in the spectra of Ag-600 and BiAg-600 indicated that the HCO_3^- species tended to only adsorb onto Ag sites. This could be closely related to the higher eCO_2RR activity against formate formation observed on BiAg-600 compared to Bi-600. A linear relationship was established between the partial current density of formate and the concentration of HCO_3^-. The fitting results yielded a quasi-one-order relationship with a coefficient of 0.76 (Fig. S18 in Supporting information). This result confirmed the direct participation of HCO_3^- in the formate formation pathway [31]. Isotopic labeling was used to clarify the nature of the protons involved during the reaction. Deuterium oxide (D_2O) was firstly employed in a CO_2 saturated solution of $D_2O + 0.5$ mol/L $KHCO_3$, where H-formate and D-formate could be produced according to the source of protons. ^1H NMR revealed that less than 5% of the protons from HCO_3^- were involved in the formate formation in the potential range of −0.55 V to −1.3 V (assuming no protons transfer between D_2O and $KHCO_3$) [8]. These findings indicates that the protons involved in the hydrogenation of OCO* species were primarily derived from H_2O activation. Thus, it was assumed that HCO_3^- acted more as a carbon source for formate rather than solely serving as a pH buffer. To validate this assumption, two control tests were conducted. Firstly, constant-potential tests were performed on BiAg-600 and Bi-600 in a CO_2 saturated phosphate buffer (0.5 mol/L, pH 7) with HCO_3^- concentrations, $C(HCO_3^-)$, below 0.14 mol/L. The obtained $FE_{formate}$ was significantly lower compared to that in the CO_2 saturated $KHCO_3$ solution (Fig. S19 and Note S4 in Supporting information), especially at high overpotential (η). Secondly, constant-potential electrolysis experiments were carried out in an Ar-saturated $KHCO_3$ solution at −0.8 V. Under these conditions, a non-negligible amount of formate was detected, corresponding to 38.7% and 18.7% $FE_{formate}$ for BiAg-600 and Bi-600, respectively. These data confirmed that HCO_3^- adsorbed on Ag sites participate directly in formate generation and promote

$FE_{formate}$ in a broad potential window. It should be noted that there were no peak related to HCO_3^- or CO_3^{2-} species on the BiAg-600 IR spectra under Ar- (Fig. S17). This indicates that the signals of HCO_3^{*-} and CO_3^{*2-} on Ag sites were attributed to the presence of molecular CO_2, as described by Eq. 1. It can be inferred that HCO_3^- species behaves as a mediator for the transfer of CO_2 from the electrolyte to the catalyst's surface, following Eqs. 1–3. The appearance of the CO_3^{2-} band near 1396 cm^{-1} only in the spectra of BiAg-600 suggests that the local pH near the surface of BiAg-600 was higher compared to Bi-600 [7]. This is because CO_3^{2-} is formed through the dehydrogenation of HCO_3^- in response to the local pH increase near the electrode's surface, as described by Eq. 4 [32]. Based on the combined findings from ATR-FTIR and isotopic labeling experiments, we propose that CO_2 reacts with water to form HCO_3^-. Simultaneously, Ag sites adsorb HCO_3^- species and releases CO_2 through a rapid equilibrium (Eqs. 2 and 3), resulting in a high local concentration of CO_2 and an increase in the local pH (Eq. 5) near the Bi sites.

$$CO_2 + H_2O \leftrightarrow HCO_3^- + H^+ \quad (1)$$

$$HCO_3^- + H_2O \leftrightarrow H_2CO_3 + OH \quad (2)$$

$$H_2CO_3 \leftrightarrow CO_2 + H_2O \quad (3)$$

$$HCO_3^- + OH^- \rightarrow CO_3^{2-} + H_2O \quad (4)$$

$$CO_2^{*\bullet-} + H_2O \rightarrow OCHO^* + OH \quad (5)$$

Due to the elevated local pH and localized CO_2 concentration, HER is impeded, leading to a sustained high activity for eCO_2RR even at highly negative potentials (below −1.3 V).

In situ SHINERS was employed to monitor the nature of the species on the catalysts' surface during the eCO_2RR, specifically focusing on the Raman region below 1000 cm^{-1}. The Bi-O stretching near 236 cm^{-1} appeared at the open circuit potential (OCP) and disappeared after applying the reaction potential, Fig. 4c, confirming that Bi oxide was present on the catalyst's surface and then reduced into metallic Bi during eCO_2RR. As the applied potential underwent a negative shift (Fig. 4d) four peaks were observed, with their assignments summarized in Table S4 (Supporting information). The Raman shift frequency at around 1019 cm^{-1} was assigned to the $\nu_{(C-OH)}$ vibration of adsorbed HCO_3^- [33,34]. Notably, the higher band intensity of HCO_3^{*-} species on BiAg-600 compared to Bi-600 demonstrated that Ag phase could easily adsorb HCO_3^{*-} species on its surface. The $\nu_{(OCHO)}$ peak near 1440 cm^{-1} corresponded to the O-bound bidentate formate adsorbed on catalyst sites [35]. The intensity of $\nu_{(OCHO)}$ on BiAg-600 was slightly lower than that on Bi-600, particularly at low η. These findings suggested that a larger amount of formate could be generated on the latter catalyst. Based on the downshift of the d-band for Bi over BiAg-600, as revealed by the CO_{ad} shift in the *in situ* FTIR spectra, the decreased oxophilicity of BiAg-600 resulted in efficient desorption of the final product formate from the active sites, facilitating subsequent CO_2 reduction and leading to an enhanced $j_{formate}$.

By considering the spectroscopic results from the *in situ* operando analyses, the mechanism of eCO_2RR on the BiAg-600 catalyst can be well understood. The Ag sites effectively captures CO_2 molecules through a continuous process of HCO_3^- consumption, regeneration (or migration), and subsequent CO_2^* adsorption. The captured CO_2^* species then accept the first electron to form $CO_2^{*\bullet-}$, which is further hydrogenated to $^*OCHO^-$ on the Bi sites, leading then to the formation of formate.

Our study contributes to understand how to improve the catalytic stability against eCO_2RR for formate synthesis and could lead to the development of novel catalysis which will help to tackle the climate change by producing value-added molecules for chemical industries.

Declaration of competing interest

The authors declare that they have no known competing financial interests or personal relationships that could have appeared to influence the work reported in this paper.

CRediT authorship contribution statement

Yaoyin Lou: Writing – review & editing, Writing – original draft, Visualization, Validation, Supervision, Investigation, Formal analysis, Data curation, Conceptualization. **Xiaoyang Jerry Huang:** Writing – review & editing, Writing – original draft, Visualization, Validation, Supervision, Investigation, Formal analysis, Conceptualization. **Kuang-Min Zhao:** Validation, Formal analysis. **Mark J. Douthwaite:** Visualization. **Tingting Fan:** Visualization, Formal analysis. **Fa Lu:** Visualization, Validation, Formal analysis. **Ouardia Akdim:** Writing – review & editing, Writing – original draft, Visualization, Validation, Supervision, Investigation, Formal analysis, Conceptualization. **Na Tian:** Visualization, Validation, Formal analysis. **Shigang Sun:** Visualization, Validation, Funding acquisition, Formal analysis. **Graham J. Hutchings:** Funding acquisition, Visualization, Validation, Formal analysis.

Acknowledgments

The authors would like to thank the Max Planck Centre for Fundamental Heterogeneous Catalysis (FUNCAT) for financial support. The authors acknowledge funding from the National Natural Science Foundation of China (No. 22002131) and China Postdoctoral Science Foundation (No. 2020M671963). We are thankful to the Beijing Synchrotron Radiation Facility (1W1B, BSRF) for help with characterizations.

Supplementary materials

Supplementary material associated with this article can be found, in the online version, at doi:10.1016/j.cclet.2024.110300.

References

[1] Adoption of the Paris Agreement Conference of the Parties to the United Nations Framework Convention On Climate Change, Paris, 2015, pp. 1–32.
[2] B.H. Ren, G.B. Wen, R. Gao, et al., Nat. Commun. 13 (2022) 2486.
[3] Y. Shi, J. Li, C. Mao, et al., Nat. Commun. 12 (2021) 5923.
[4] Y. Guan, J. Yan, Y. Liu, et al., J. Catal. 424 (2023) 211–220.
[5] L. Li, Y. Zhang, X. Luo, et al., J. Catal. 86 (2023) 569–578.
[6] M. Jouny, W. Luc, F. Jiao, Ind. Eng. Chem. Res. 57 (2018) 2165–2177.
[7] J. Zhang, T. Fan, P. Huang, et al., Adv. Funct. Mater. 32 (2022) 2113075.
[8] W. Ma, S. Xie, X.G. Zhang, et al., Nat. Commun. 10 (2019) 892.
[9] D. Wu, X. Wang, X.Z. Fu, J.L. Luo, Appl. Catal. B: Environ. 284 (2021) 119723.
[10] Y. Wang, Y. Li, J. Liu, et al., Angew. Chem. Int. Ed. 60 (2021) 7681–7685.
[11] L. Peng, C. Chen, R. He, et al., EcoMat 4 (2022) e12260.
[12] J. Yan, Y. Guan, B. Marchetti, et al., Chem. Eng. J. 467 (2023) 143531.
[13] L. Peng, W. Lou, L. Li, et al., Sep. Purif. Technol. 330 (2024) 125372.
[14] E. Zhang, T. Wang, K. Yu, et al., J. Am. Chem. Soc. 141 (2019) 16569–16573.
[15] A.K. Inge, M. Köppen, J. Su, et al., J. Am. Chem. Soc. 138 (2016) 1970–1976.
[16] J. Di, P. Song, C. Zhu, et al., ACS Mater. Lett. 2 (2020) 1025–1032.
[17] S. Liu, J. Xiao, X.F. Lu, et al., Angew. Chem. Int. Ed. 58 (2019) 8499–8503.
[18] E.L. Clark, C. Hahn, T.F. Jaramillo, A.T. Bell, J. Am. Chem. Soc. 139 (2017) 15848–15857.
[19] K. Jiang, P. Kharel, Y. Peng, et al., ACS Sustain. Chem. Eng. 5 (2017) 8529–8534.
[20] X.D. Liang, Q.Z. Zheng, N. Wei, et al., Nano Energy 114 (2023) 108638.
[21] W. Luc, C. Collins, S. Wang, et al., J. Am. Chem. Soc. 139 (2017) 1885–1893.
[22] L. Vitos, A.V. Ruban, H.L. Skriver, J. Kollár, Surf. Sci. 411 (1998) 186–202.
[23] V.F. Ruiz-Ruiz, I. Zumeta-Dubé, D. Díaz, M.J. Arellano-Jiménez, M. José-Yacamán, J. Phys. Chem. C 121 (2017) 940–949.

[24] A. Christensen, A.V. Ruban, P. Stoltze, et al., Phys. Rev. B 56 (1997) 5822–5834.
[25] P.T. Sprunger, E. Lægsgaard, F. Phys. Rev. B 54 (1996) 8163–8171.
[26] S. He, F. Ni, Y. Ji, et al., Angew. Chem. Int. Ed. 57 (2018) 16114–16119.
[27] D. Yao, C. Tang, A. Vasileff, et al., Angew. Chem. Int. Ed. 60 (2021) 18178–18184.
[28] C.W. Lee, N.H. Cho, K.D. Yang, K.T. Nam, ChemElectroChem 4 (2017) 2130–2136.
[29] Z. Tao, A.J. Pearce, J.M. Mayer, H. Wang, J. Am. Chem. Soc. 144 (2022) 8641–8648.
[30] B.A. Lu, L.F. Shen, J. Liu, et al., ACS Catal. 11 (2021) 355–363.
[31] K. Fan, Y. Jia, Y. Ji, et al., ACS Catal. 10 (2020) 358–364.
[32] M. Dunwell, X. Yang, B.P. Setzler, et al., ACS Catal. 8 (2018) 3999–4008.
[33] W.W. Rudolph, G. Irmer, E. Königsberger, Dalton Trans. 7 (2008) 900–908.
[34] S. Kai, W. Chaozhi, X. Guangzhi, Spectrochim. Acta A 45 (1989) 1029–1032.
[35] D. Bohra, I. Ledezma-Yanez, G. Li, et al., Angew. Chem. Int. Ed. 58 (2019) 1345–1349.